IEEE Access
Multidisciplinary | Rapid Review | Open Access Journal

Received February 16, 2020, accepted March 7, 2020, date of publication March 11, 2020, date of current version March 26, 2020.

Digital Object Identifier 10.1109/ACCESS.2020.2980058

Low-Rank Tensor Completion and Total Variation Minimization for Color Image Inpainting

MENGJIE QIN[1], ZHUORONG LI[2], SHENGYONG CHEN[3], (Senior Member, IEEE), QIU GUAN[1], AND JIANWEI ZHENG[1]

[1]College of Computer Science and Engineering, Zhejiang University of Technology, Hangzhou 310014, China
[2]School of Computer and Computing Science, Zhejiang University City College, Hangzhou 310015, China
[3]College of Computer Science and Engineering, Tianjin University of Technology, Tianjin 300222, China

Corresponding author: Jianwei Zheng (zjw@zjut.edu.cn)

This work was supported in part by the National Key Research and Development Program of China under Grant 2018YFE0126100, and in part by the Natural Science Foundation of Zhejiang Province under Grant LY19F030016.

ABSTRACT Low-rank (LR) and total variation (TV) are two most frequent priors that occur in image processing problems, and they have sparked a tremendous amount of researches, particularly for moving from scalar to vector, matrix or even high-order based functions. However, discretization schemes used for TV regularization often ignore the difference of the intrinsic properties, so it will lead to the problem that local smoothness cannot be effectively generated, let alone the problem of blurred edges. To address the image inpainting problem with corrupted data, in this paper, the color images are naturally considered as three-dimensional tensors, whose prior of smoothness can be measured by varietal TV norm along different dimensions. Specifically, we propose incorporating Shannon total variation (STV) and low-rank tensor completion (LRTC) into the construction of the final cost function, in which a new nonconvex low-rank constraint, namely truncated γ-norm, is involved for closer rank approximation. Moreover, two methods are developed, i.e., LRRSTV and LRRSTV-T, due to the fact that LRTC can be represented by tensor unfolding and tensor decomposition. The final solution can be achieved by a practical variant of the augmented Lagrangian alternating direction method (ALADM). Experiments on color image inpainting tasks demonstrate that the proposed methods perform better then the state-of-the-art algorithms, both qualitatively and quantitatively.

INDEX TERMS Tensor completion, truncated γ-norm, tensor decomposition, Shannon total variation, image inpainting.

I. INTRODUCTION

In the fields of computer vision and image processing [1], image inpainting is a vital research topic which can be regarded as a missing value estimation problem. And its main challenge is how to establish relations between known and unknown elements. Some methods often used in image inpainting [2], i.e., PDEs [3] and belief Propagation [4], mainly focus on the local relationship. The fundamental supposition is that the missing items are lied in adjacent elements. Therefore, it is known that the further away two pixels are, the less correlated they would be. However, it is a fairly common occasion in the natural images that the missing items may depend on those elements that are far away from themselves. Meanwhile, the convolutional neural networks (CNNs)-based approaches [5], [6] have been proved to be particularly successful because of its powerful learning ability, which performs excellently in the representation of hierarchical non-linear images. However, there are a huge amount of tuning parameters in the CNN models [7], [8], and implementing the CNN algorithms usually require a large number of training data sets as well as strong compression capabilities. As for the small-sized scenarios, especially the single picture application in this paper, the advantage of CNN models cannot be fully employed. Thus, it is still necessary to develop new prior-based algorithms that can capture intrinsic information from the images.

Matrix completion (MC) [9], namely the second-order tensor completion problem [10], has been reported to be able to effectively estimate the missing values in a matrix in line

The associate editor coordinating the review of this manuscript and approving it for publication was Peng Liu.

with a small number of known items. Although MC is widely used in image/video inpainting, denoising [11] and decoding problems, it suffers from unlimited solutions due to its ill-poseness without using any prior constraints [12]. A general assumption is that for a image to be completed, its matrix rank should be probably as low as possible. Accordingly, a common scheme is to minimize the difference between the given incomplete matrix and the estimated one by using the low-rank constraint. Therefore, it is often substituted by nuclear norm(NN) which is continuous, convex and easy to optimize [13]. In fact, it has been proved that NN is the tightest convex approximation of the rank function among all existing surrogates [14].

In implementation, nuclear norm is set as ℓ_1-norm on the vector of singular values. It gets low-rankness through encouraging the sparsity of singular values. As Fan and Li pointed out [15], the ℓ_1-norm was a loose approximation to the ℓ_0-norm and, it over penalized large entries of vectors. Hence, when we draw an analogy between the ℓ_0-norm of vectors and the rank function of matrices, we can see that the larger singular values are also over penalized. Schatten-p quasi-norm ($0 < p < 1$) [16] was suggested to replace the nuclear norm for better approximating the rank function. Recently, some novel low rank approximation methods have also been proposed, e.g., the weighted Schatten-p norm and the truncated nuclear norm. Besides, Ref. [17] proposed a γ-norm based low-rank regularizer that is totally different from Schatten-p norm and held more preferable low-rank property.

Tensor is a generalization of matrix and vector, which is convictive to show multidimensional data or interactions relevant to multiple factors. A third-order tensor is well suited to describe three channels, i.e., height, width and color, of a natural image. In recent years, different variants of low rank constraints have also been presented to recover higher-order tensors from given observations. The main difference lies in the detailed definition on the rank of used tensors. Accordingly, many methods of low-rank tensor completion (LRTC) [18] are accomplished by extending the definition of the rank of a matrix. The first LRTC definition was proposed by Liu et al [18]. In their works, the nuclear norm of a tensor was computed as an average of all NN values from its unfolded matrices. The resulted model was then optimized by minimizing the averaged constraint of the restored tensor. However, since it shared the same entries for all the unfolded matrices in each mode, their nuclear norms were interdependent consequently. Thus, the defined tensor nuclear norm was difficult to minimize. To address this issue, Ref. [18] introduced several auxiliary matrices for different modes to separate the interdependent terms in optimization. As a result, they established two enhanced methods, FaLRTC and HaLRTC. Meanwhile, the other approaches used tensor decomposition techniques, which have been proposed in Ref. [19]. For the decomposition technique used in LRTC, some methods based on Tucker decomposition are widely proposed. For example, Ref. [20] developed a method that employs nuclear norm for the factors of Tucker decomposition, called as LRTC-TV-II. Tucker-based methods can obtain a good performance by minimizing the total variation and Trucker-rank constraints, but there may be redundancy in the core tensor and need further decomposition [21]. The other line of tensor completion methods directly minimize the CANECOMP/PARAFAC(CP) rank, which is another natural extension of matrix rank. Ref. [22] proposed fully Bayesian CANECOMP/PARAFAC (FBCP) method, which uses the Bayesian inference to find an appropriate tensor rank. The methods based on CP decomposition have better accuracy, but the rank-1 approximation of step-by-step operation is inefficient [23].

In our paper, we consider that low-rank constraints, though useful, are not sufficient to effectively utilize some potential local structures of tensors for completion. This point is especially evident in image inpainting. Due to the existence of objects or edges, visual data tend to show smooth and segmented structure in spatial dimension. Without special considerations on the local structures, the recovered results may be barely satisfactory. Since total variation (TV) regularization was proposed for image recovery [24], it has been proven extremely useful for many applications like image inpainting, interpolation [12], artifacts removal [25], [26] and so forth. Recently, Remy Abergel and Lionel Moisan proposed the Shannon Total Variation (STV) [27] that performed better in aspects of artifact removal, isotropy and sub-pixel accuracy. According to the Riemann sum of corresponding integrals, the continuous TV of the Shannon interpolation can be closely approximated by STV. Borrowing their idea and following the low rank property of the natural images, we attempt to combine these two terms in one cost function for practical image inpainting.

The main contributions of the paper can be summarized as follows: 1) In this work, to enhance performance, we take the local smoothness and the global structure into consideration and propose our tensor completion method. Note that, to the best of our knowledge, the STV has never been investigated for tensor completion. For the purpose of capturing most low-rank complementary information, STV is introduced into tensor recovery to further discover the local piecewise smooth structure. 2) We present a new low-rank regularizer, namely truncated γ-norm, which is an operator for a better approximation to the true rank minimization problem. 3) As tensor completion can be formulated by both tensor unfolding and tensor decomposition, we propose two image inpainting approaches using direct tensor modeling techniques. In this way, we can infer the multichannel factors and the predictive distribution over missing entries given an incomplete tensor. 4) To solve the nonconvex optimization problem in our algorithm, we propose an efficient algorithm involving augmented Lagrangian alternating direction method(ALADM) [28]and proximal gradient, which can efficiently deliver the completion results of our method. 5) The experimental images can be recovered by the proposed methods generating certain smoothly changed shape comparable

to that of the original images. Two well-known numerical indicators, i.e., Peak Signal to Noise Ratio (PSNR) and Structural Similarity (SSIM), are used to quantitatively evaluate our approaches.

II. RELATED WORK

A. A SIMPLE FORMULATION OF TENSOR COMPLETION

Given $\boldsymbol{M} \in \mathbb{R}^{p\times q}$ whose elements in the set Ω are known while the remaining elements are missing, a general matrix completion problem can be written as follows [29]:

$$\min_{\boldsymbol{X}} \frac{1}{2} \|\boldsymbol{X}_\Omega - \boldsymbol{M}_\Omega\|_F^2 + \tau \|\boldsymbol{X}\|_* \tag{1}$$

where $\boldsymbol{X}$ is the target matrix to be recoved and τ is a constant, $\|\cdot\|_F^2$ is Frobenius norm. Ref. [18] extends the matrix nuclear norm to the tensor case and proposes to recover the missing entries in a low rank tensor by solving nuclear norm minimization problem.

$$\min_{\boldsymbol{\mathcal{X}}} \frac{1}{2} \|\boldsymbol{\mathcal{X}}_\Omega - \boldsymbol{\mathcal{Y}}_\Omega\|_F^2 + \tau \|\boldsymbol{\mathcal{X}}\|_* \tag{2}$$

where $\boldsymbol{\mathcal{X}},\boldsymbol{\mathcal{Y}} \in \mathbb{R}^{I_1\times\ldots\times I_n}$ are n-mode tensors with identical size in each mode, the nuclear norm of tensor $\boldsymbol{\mathcal{X}}$ is defined as $\|\boldsymbol{\mathcal{X}}_{(i)}\|_* := \sum_{i=1}^n \alpha_i \|\boldsymbol{X}_{(i)}\|_*$, and α_is are constants satisfying $\alpha_i \geq 0, \sum_{i=1}^n \alpha_i = 1$. Under this definition, the optimization in (2) can also be written as

$$\min_{\boldsymbol{\mathcal{X}}} \sum_{i=1}^n \alpha_i \left\|\boldsymbol{\mathcal{X}}_{(i)}\right\|_* \quad s.t.\ \boldsymbol{\mathcal{X}}_\Omega = \boldsymbol{\mathcal{Y}}_\Omega \tag{3}$$

Both the problems (2) and (3) are difficult to solve due to the interdependent matrix nuclear norm terms, i.e., while we optimize the sum of multiple matrix nuclear norms, these matrices share the same entries and cannot be optimized independently. The key motivation of simplifying this issue is to split these interdependent terms so that they can be solved independently. In related studies, Ji Liu el.at propose High Accuracy Low Rank Tensor Completion (HaLRTC) algorithm [18]. Specifically, they introduce additional matrices $\boldsymbol{M}_{(1)}, \ldots, \boldsymbol{M}_{(n)}$ and obtained the following equivalent formulation:

$$\begin{aligned} &\min_{\boldsymbol{\mathcal{X}}, \{\boldsymbol{M}_{(i)}\}_{i=1}^n} \sum_{i=1}^n \alpha_i \left\|\boldsymbol{M}_{(i)}\right\|_* \\ &s.t. \boldsymbol{\mathcal{X}}_\Omega = \boldsymbol{\mathcal{Y}}_\Omega, \{\boldsymbol{\mathcal{X}}_{(i)} = \boldsymbol{M}_{(i)}\}_{i=1}^n \end{aligned} \tag{4}$$

where $\boldsymbol{M}_{(i)} \in \mathbb{R}^{I_i\times(\prod_{k\neq i} I_k)}$, and $\boldsymbol{\mathcal{X}},\boldsymbol{\mathcal{Y}} \in \mathbb{R}^{I_1\times\ldots\times I_n}$.

B. LOW-RANK TENSOR COMPLETION WITH TV

Theoretically, within lower bound of the rank function of matrices, the nuclear norm is the tightest convex. Thus, NN is always adopted as a practical measurement of rank, which can be further used to represent the low rank prior. Moreover, according to the case discussed in the introduction section, this work also considers the sparse gradient regularization. Altogether we have the following formulation:

$$\begin{aligned} &\min_{\boldsymbol{\mathcal{X}}, \{\boldsymbol{M}_{(i)}\}_{i=1}^n} \sum_{i=1}^n \alpha_i \left\|\boldsymbol{M}_{(i)}\right\|_* + \sum_{i=1}^n \lambda \|\nabla \boldsymbol{M}_{(i)}\|_0 \\ &s.t. \boldsymbol{\mathcal{X}}_\Omega = \boldsymbol{\mathcal{Y}}_\Omega, \{\boldsymbol{\mathcal{X}}_{(i)} = \boldsymbol{M}_{(i)}\}_{i=1}^n \end{aligned} \tag{5}$$

Noticing the second term in equation (5) is the ℓ_0-norm of gradient. Minimization corresponding to the ℓ_0-norm is usually relaxed to ℓ_1-norm and thus the ℓ_0- gradient becomes total variation [30]. Similar to the rank function, the ℓ_0-norm is strongly non-convex, which turns to be convex by relaxing itself to total variation. Borrowing the scheme of LRTV, we also incorporate total variation into our image inpainting problem. Consequently, Eq. (5) can be reformulated as follows.

$$\begin{aligned} &\min_{\boldsymbol{\mathcal{X}}, \{\boldsymbol{M}_{(i)}\}_{i=1}^n} \sum_{i=1}^n \alpha_i \left\|\boldsymbol{M}_{(i)}\right\|_* + \sum_{i=1}^n \lambda \mathrm{TV}(\boldsymbol{M}_{(i)}) \\ &s.t. \boldsymbol{\mathcal{X}}_\Omega = \boldsymbol{\mathcal{Y}}_\Omega, \{\boldsymbol{\mathcal{X}}_{(i)} = \boldsymbol{M}_{(i)}\}_{i=1}^n \end{aligned} \tag{6}$$

Compared with the cost function that only has the low rank regularization term, the TV regularization can improve the restoration effect. However, there are some drawbacks of the original TV regularization. First, it often smooths out the true depth of the edges. Second, it can be observed that TV norm always becomes close or even lower than the truth in the depth of inpainting effects. Third, even with a lower-than-groundtruth TV, the image is still visually noisy.

C. THE SHANNON TOTAL VARIATION

For the total variation property, most algorithms choose to approximate the continuous TV by a sum (over all pixels) of the ℓ_2 norm of a discrete finite-difference estimate in the image gradient, that is,

$$\mathrm{TV}^d(u) = \sum_{(i,j)\in\Omega} \sqrt{(\partial_1 u(i,j))^2 + (\partial_2 u(i,j))^2} \tag{7}$$

where

$$\begin{cases} \partial_1 u(i,j) = u(i+1,j) - u(i,j) \\ \partial_2 u(i,j) = u(i,j+1) - u(i,j) \end{cases} \tag{8}$$

In some situations, an anisotropic scheme (ℓ_1 norm) may be used [31], leading to the anisotropic discrete TV that can be written as

$$\mathrm{TV}_{ani}^d(u) = \sum_{(i,j)\in\Omega} |\partial_1 u(i,j)| + |\partial_2 u(i,j)| \tag{9}$$

The performances of these numerical schemes are poor both in pixel-level and subpixel-level. In fact, it is difficult to interpolate on the image, which obtained either by minimizing TV^d-based energies, or sampled based on Shannon theory. Recently, Remy Abergel and Lionel Moisan proposed a new total variation termed as the Shannon Total Variation (STV) to relieve this issue.

Let $|\cdot|$ denotes the ℓ^2 norm over $\mathbb{R}^2$, let $\Omega = I_p \times I_Q$ denotes a 2-D discrete domain of size $P \times Q$ and $u \in \mathbb{R}^\Omega$,

a discrete gray-level image with domain Ω. We define the Shannon Total Variation of u by

$$\mathrm{STV}_\infty(u) = \int_{[0,P]\times[0,Q]} |\nabla U(x,y)| dxdy \tag{10}$$

in which U is the Shannon interpolation of u, and the gradient of the trigonometric polynomial U is denoted by $\nabla U : \mathbb{R}^2 \to \mathbb{R}^2$. Therefore, there is no closed-form formula for (10), then Remy Abergel and Lionel Moisan approximated this continuous integral with the Riemann sum

$$\mathrm{STV}_a(u) = \frac{1}{a^2} \sum_{(i,j)\in\Omega_a} |\nabla u(i,j)| \tag{11}$$

where $n \in \mathbb{N}^*$, $\Omega_a = I_{aP} \times I_{aQ}$, and $\forall (i,j) \in \Omega_a, \nabla u(i,j) = \nabla U(\frac{i}{a}, \frac{j}{a})$.

In order to calculate $\mathrm{STV}_a(u)$, we can get the gradient of U, that is, $\forall (i,j) \in \mathbb{R}^2$

$$\nabla U(i,j) = \frac{1}{PQ} \sum_{\substack{-P/2\le\alpha\le P/2 \\ -Q/2\le\beta\le Q/2}} e^{2\iota\pi(\frac{\alpha i}{P}+\frac{\beta j}{Q})} g_{\hat{u}}(\alpha,\beta) \tag{12}$$

where

$$\hat{u}(\alpha,\beta) = \sum u(i,j) e^{-2\iota\pi(\frac{\alpha i}{P}+\frac{\beta j}{Q})} \tag{13}$$

$$g_{\hat{u}}(\alpha,\beta) = 2\iota\pi\varepsilon_p(\alpha)\varepsilon_Q(\beta)\hat{u}(\alpha,\beta) \begin{pmatrix} \alpha/P \\ \beta/Q \end{pmatrix} \tag{14}$$

and the definition for integer P

$$\varepsilon_p(\alpha) = \begin{cases} \frac{1}{2}, & |\alpha| = \frac{P}{2} \\ 1, & \text{otherwise} \end{cases} \tag{15}$$

About the dual formulation of the Shannon total variation, the STV_n operator defined in (11) can be rewritten under the form $\mathrm{STV}_n(u) = \frac{1}{n^2}\|\nabla_n U\|_{1,2}$, where $\|\cdot\|_{1,2}$ is the norm over the space $\mathbb{R}^{\Omega_a} \times \mathbb{R}^{\Omega_a}$ which is defined as

$$\forall g \in \mathbb{R}^{\Omega_a} \times \mathbb{R}^{\Omega_a}, \|g\|_{1,2} = \sum_{(i,j)\in\Omega_a} |g(i,j)| \tag{16}$$

One can easily checks that the dual norm of $\|\cdot\|_{1,2}$ is the norm $\|\cdot\|_{\infty,2}$ defined as

$$\forall p \in \mathbb{R}^{\Omega_a} \times \mathbb{R}^{\Omega_a}, \|p\|_{\infty,2} = \max_{(i,j)\in\Omega_a} |p(i,j)| \tag{17}$$

For any integer $a \ge 1$ and for any matrix or tensor $u \in \mathbb{R}^\Omega$,

$$\mathrm{STV}_a(u) = \max_{p\in\mathbb{R}^{\Omega_a}\times\mathbb{R}^{\Omega_a}} \langle \frac{1}{a^2}\nabla_a u, p\rangle - \delta_{\|\cdot\|_{\infty,2}\le 1}(p) \tag{18}$$

and $\delta_{\|\cdot\|_{\infty,2}\le 1} = \begin{cases} 0, & \|p\|_{\infty,2} \le 1 \\ +\infty, & \text{otherwise} \end{cases}$.

The studies of Remy Abergel and Lionel Moisan show that it is difficult to interpolate on the processed images based on the variational TV when the TV is discretized by the classical finite difference scheme. Among them, STV successfully addresses this issue. Fig. 1 shows the recovery results of (a) by TV and STV. When magnifying the images, compared with (d), (c) is more blurred and noncontinuous. So, we can absolutely believe that STV will also perform better than traditional TV algorithms in our algorithm model.

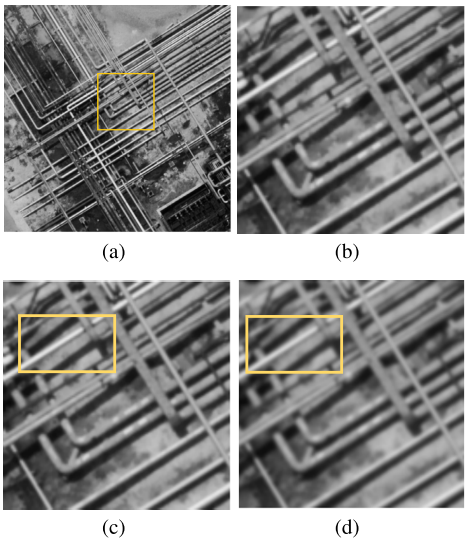

FIGURE 1. A simple image restoration instance on 40% random missing. (a-b) the original. (c) recovery results by STV. (d) recovery results by TV.

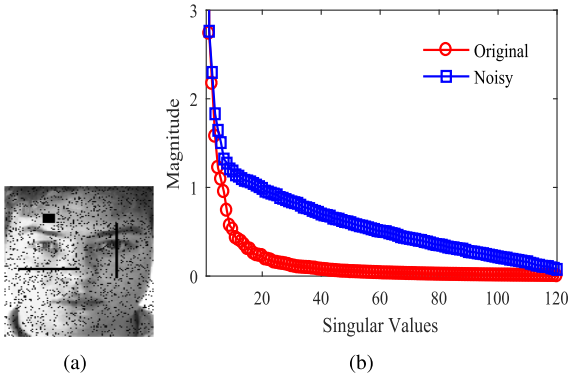

FIGURE 2. An instance of (a) corrupted sample and (b) its rank components.

III. PROPOSED MODEL: LRRSTV

A. PROBLEM FORMULATION

In the previous section we have discussed the low rank tensor completion problem and the STV constraint. Generally speaking, low-rank regularization is used to retrieve useful information from remote regions, while total variation regularization for keeping better local consistency. As discussed in the end of subsection II. C, we will replace TV constraint with STV constraint to reformulate equation (6) as follows

$$\begin{aligned} &\min_{\boldsymbol{\mathcal{X}},\{\boldsymbol{M}_{(i)}\}_{i=1}^n} \sum_{i=1}^n \alpha_i \left\|\boldsymbol{M}_{(i)}\right\|_* + \sum_{i=1}^n \lambda \mathrm{STV}(\boldsymbol{M}_{(i)}) \\ &s.t. \boldsymbol{\mathcal{X}}_\Omega = \boldsymbol{\mathcal{Y}}_\Omega, \{\boldsymbol{\mathcal{X}}_{(i)} = \boldsymbol{M}_{(i)}\}_{i=1}^n \end{aligned} \tag{19}$$

Recall that for the first constraint in equation (19), existing methods usually employ NN to recover the low rank structure. However, there is still a gap between current research and practical application. The solution obtained by those existing algorithms usually deviates from the original problem.

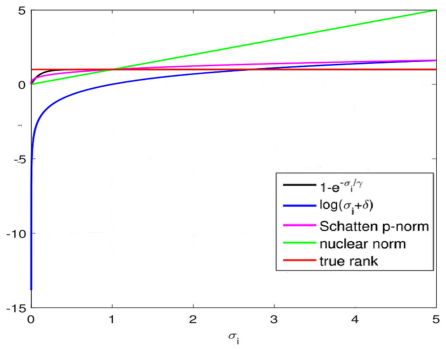

FIGURE 3. Approximation of the rank function using different functions.

In other words, although the nuclear norm used in model (19) is the tightest convex surrogate to the rank constraint, the obtained solution is only a loose approximation to the original one, particularly in the presence of noises. Fig. 2 illustrates a noisy face image and its rank components. Fig. 2(b) shows that the larger rank components of the noisy image are closely coherent with the original ones, while the smaller singular values deviate far away from the original ones. Based on these observations, we propose truncated γ-norm by only minimizing the smallest $\min(p, q) - r$ singular values, where $\min(p, q)$ is the number of singular values and r is the main action of the matrix, which is defined as

$$\text{rank}(\boldsymbol{M}) \approx \|\boldsymbol{M}\|_{\gamma,r} = \sum_{s=r+1}^{\min(p,q)} (1 - e^{-\sigma_s(\boldsymbol{M})/\gamma}) \tag{20}$$

where $\gamma > 0$. Here, we substitute the NN tern in (19) with our truncated γ-norm. Fig. 3 shows the behaviors of several commonly used low rank regularizers. From this figure, it can be easily observed that when the singular values are relatively larger, then the responding curves of nuclear norm, Schatten-p norm and the log-determinant function locate far away from the original one. That means they cannot approximate the rank function well. On the contrary, the γ-norm performs better than them in term of approxinating the true rank.

The proposed low rank tensor completion using truncated γ-norm and Shannon total variation regularized (LRRSTV) method is formulated as follows:

$$\begin{aligned} &\min_{\boldsymbol{\mathcal{X}},\boldsymbol{M}_{(i)}} \beta_i \sum_{i=1}^{n} \lambda \, \text{STV}(\boldsymbol{M}_{(i)}) + \frac{1}{n} \sum_{i=1}^{n} \left\|\boldsymbol{M}_{(i)}\right\|_{\gamma,r} \\ &s.t. \boldsymbol{\mathcal{X}}_\Omega = \boldsymbol{\mathcal{Y}}_\Omega, \{\boldsymbol{X}_{(i)} = \boldsymbol{M}_{(i)}\}_{i=1}^{n} \end{aligned} \tag{21}$$

where tensor $\boldsymbol{\mathcal{X}}$ represents the recovery result; $\boldsymbol{X}_{(i)}$ denotes its mode-n unfolding matrix of tensor $\boldsymbol{\mathcal{X}}$. λ is a tunable parameter; $\beta_1, \beta_2, \ldots, \beta_n$ are 0 or 1, which indicate there is a smooth piecewise prior on the n-th mode of tensors recovered by our method. The settings of $\beta_1, \beta_2, \ldots, \beta_n$ are domain dependent. when $\boldsymbol{\mathcal{Y}}$ is a three-order tensor of color image, we set $\beta_1, \beta_2 = 1$ and $\beta_3 = 0$, due to the fact that a prior that has both smoothness and piecewise continuity properties cannot exist in any dimension other than the spatial one.

B. ALGORITHM OPTIMIZATION

In our model, the two terms share the same variable $\boldsymbol{M}_{(i)}$, they are interdependent. Furthermore $\boldsymbol{M}_{(1)}, \boldsymbol{M}_{(2)}, \ldots, \boldsymbol{M}_{(n)}$ again share the same entries of tensor $\boldsymbol{\mathcal{X}}$, which makes our model difficult to optimize. Hence, we introduce two matrices $\{\boldsymbol{N}_{(i)}\}_{i=1}^{n}$ and $\{\boldsymbol{R}_{(i)}\}_{i=1}^{n}$ as auxiliary variables. Correspondingly, we split the interdependencies and rewrite the optimization problem as

$$\begin{aligned} &\min_{\boldsymbol{\mathcal{X}},\{\boldsymbol{M}_{(i)},\boldsymbol{N}_{(i)},\boldsymbol{R}_{(i)}\}_{i=1}^{n}} \beta_i \sum_{i=1}^{n} \lambda \text{STV}(\boldsymbol{N}_{(i)}) + \frac{1}{n} \sum_{i=1}^{n} \left\|\boldsymbol{M}_{(i)}\right\|_{\gamma,r} \\ &s.t. \boldsymbol{\mathcal{X}}_\Omega = \boldsymbol{\mathcal{Y}}_\Omega, \{\boldsymbol{X}_{(i)} = \boldsymbol{M}_{(i)}, \boldsymbol{N}_{(i)} = \boldsymbol{R}_{(i)}, \boldsymbol{R}_{(i)} = \boldsymbol{X}_{(i)}\}_{i=1}^{n} \end{aligned} \tag{22}$$

We follow the augmented Lagrangian alternating direction method (ALADM) algorithm to solve the cost function in equation (22). ALADM is proven to be efficient for solving optimization problems with multiple non-smooth terms in the cost function. By using the augmented Lagrange formulation, the optimization problem is transformed into:

$$\begin{aligned} \mathcal{L} = &\sum_{i=1}^{n} \lambda \left(\beta_i \text{STV}(\boldsymbol{N}_{(i)}) + \frac{\rho_1}{2} \left\| \boldsymbol{N}_{(i)} - \boldsymbol{R}_{(i)} + \frac{\Lambda_{1(i)}}{\rho_1} \right\|_F^2 \right) \\ &+ \sum_{i=1}^{n} \lambda \left(\frac{\rho_2}{2} \left\| \boldsymbol{R}_{(i)} - \boldsymbol{X}_{(i)} + \frac{\Lambda_{2(i)}}{\rho_2} \right\|_F^2 \right) \\ &+ \sum_{i=1}^{n} \left(\frac{1}{n} \|\boldsymbol{M}_{(i)}\|_{\gamma,r} + \frac{\rho_3}{2} \left\| \boldsymbol{M}_{(i)} - \boldsymbol{X}_{(i)} + \frac{\Lambda_{3(i)}}{\rho_3} \right\|_F^2 \right) \\ &s.t. \boldsymbol{\mathcal{X}}_\Omega = \boldsymbol{\mathcal{Y}}_\Omega \end{aligned} \tag{23}$$

where matrices $\{\Lambda_{1(i)}\}_{i=1}^{n}, \{\Lambda_{2(i)}\}_{i=1}^{n}, \{\Lambda_{3(i)}\}_{i=1}^{n}$ are Lagrange multipliers. Note that, although the main purpose of Lagrange method is to turn a constrained variational problem to an unconstrained one, we still retain the constraint $\boldsymbol{\mathcal{X}}_\Omega = \boldsymbol{\mathcal{Y}}_\Omega$ for directly accessing the known points. For each of the four matrices $\{\boldsymbol{M}_{(i)}\}_{i=1}^{n}, \{\boldsymbol{N}_{(i)}\}_{i=1}^{n}, \{\boldsymbol{R}_{(i)}\}_{i=1}^{n}, \{\boldsymbol{X}_{(i)}\}_{i=1}^{n}$ to be resolved in equation (23), all their subproblems are convex when the remaining three matrices are kept fixed.

In other words, equation (23) can be solved iteratively via the following four subproblems. First, by fixing $\{\boldsymbol{M}_{(i)}\}_{i=1}^{n}, \{\boldsymbol{R}_{(i)}\}_{i=1}^{n}, \{\boldsymbol{X}_{(i)}\}_{i=1}^{n}, \{\boldsymbol{N}_{(i)}\}_{i=1}^{n}$ is updated by the following formulation.

$$\min_{\{\boldsymbol{N}_{(i)}\}_{i=1}^{n}} \lambda \left(\beta_i \text{STV}(\boldsymbol{N}_{(i)}) + \frac{\rho_1}{2} \left\| \boldsymbol{N}_{(i)} - \boldsymbol{R}_{(i)} + \frac{\Lambda_{1(i)}}{\rho_1} \right\|_F^2 \right) \tag{24}$$

According to the dual formulation of the STV, and equation (24) can be written as follows:

$$\begin{aligned} \min_{\{\boldsymbol{N}_{(i)}\}_{i=1}^{n}} \lambda \left(\left\langle \frac{\beta}{n^2} \nabla_n \boldsymbol{N}_{(i)}, p_{(i)} \right\rangle - \delta_{\|\cdot\|_{\infty,2} \le 1}(p_{(i)}) \right) \\ + \lambda \frac{\rho_1}{2} \left\| \boldsymbol{N}_{(i)} - \boldsymbol{R}_{(i)} + \frac{\Lambda_{1(i)}}{\rho_1} \right\|_F^2 \end{aligned} \tag{25}$$

We adopt the Chambolle-Pock (CP) algorithm [32] to resolve Eq.(25) due to its complexity. CP has been widely

used in all kinds of image processing assignments involving total variation and it shows good convergence in practical applications. Generally speaking,the CP algorithm is developed for the problems shown below.

$$\min_x \max_y \left\{ \langle Kx, y\rangle + G(x) - F^*(y) \right\} \tag{26}$$

By drawing parallel to (26), equation (25) can be similarly optimized with $(x, y) = (\boldsymbol{N}_{(i)}, p_{(i)})$, $K = \frac{\beta}{n^2}\nabla_n$, $G(\boldsymbol{N}_{(i)}) = \frac{\rho_1}{2}\left\|\boldsymbol{N}_{(i)} - \boldsymbol{R}_{(i)} + \frac{\Lambda_{1(i)}}{\rho_1}\right\|_F^2$, and $F^*(p_{(i)}) = \delta_{\|\cdot\|_{\infty,2}\le 1}(p_{(i)})$. In Algorithm 1, we list the optimization procedure for problem (24), where the proximal mapping of prox_σ and prox_τ can be formulated as follows.

$$\text{prox}_\sigma[F^*](z) = \arg\min_{z'} \left\{ F^*(z') + \frac{\|z - z'\|_F^2}{2\sigma} \right\} \tag{27}$$

Algorithm 1 Chambolle-Pock(CP) Resolvent Algorithm for Problem (24)

1: $\tau, \sigma > 0; \theta \in [0, 1]; k = 0$
2: Initialize $\boldsymbol{N}_{(i)}, p_{(i)}$ to zero values
3: $\bar{\boldsymbol{N}}_{(i)}^0 = \boldsymbol{N}_{(i)}^0$
4: Repeat
5: $p_{(i)}^{k+1} = \text{prox}_\sigma[F^*]\left(p_{(i)}^k + \sigma K \bar{\boldsymbol{N}}_{(i)}^k\right)$
6: $\boldsymbol{N}_{(i)}^{k+1} = \text{prox}_\tau[G]\left(\boldsymbol{N}_{(i)}^k - \tau K^T p_{(i)}^{k+1}\right)$
7: $\bar{\boldsymbol{N}}_{(i)}^{k+1} = \boldsymbol{N}_{(i)}^{k+1} + \theta\left(\boldsymbol{N}_{(i)}^{k+1} - \boldsymbol{N}_{(i)}^k\right)$
8: $k = k + 1$

In Algorithm 1, in the case $\theta = 0$, one iteration k consists in a proximal ascent of $p_{(i)} \mapsto H(\boldsymbol{N}_{(i)}^k, p_{(i)})$ followed by a proximal descent of $\boldsymbol{N}_{(i)} \mapsto H(\boldsymbol{N}_{(i)}, p_{(i)}^{k+1})$, producing a semi-implicit variant of the classic Arrow-Hurwicz algorithm within $O(1/\sqrt{T})$ after T iterations. In the case $\theta = 1$, let $L = \|\frac{\beta}{n^2}\nabla_n\|$ satisfy $\tau\sigma L^2 < 1$ and assume problem (26) has a saddle-point. The iterate $\bar{\boldsymbol{N}}_{(i)}^{k+1} = \boldsymbol{N}_{(i)}^{k+1} + \theta\left(\boldsymbol{N}_{(i)}^{k+1} - \boldsymbol{N}_{(i)}^k\right)$ represents the linear approximation of the next iteration $\boldsymbol{N}_{(i)}^{k+2}$ based on the previous iterates $\boldsymbol{N}_{(i)}^{k+1}$ and $\boldsymbol{N}_{(i)}^k$.It is generally used to make the scheme more implicit and to prove the convergence of the sequence $(\boldsymbol{N}_{(i)}^k, p_{(i)}^k)$ towards the saddle-point with an estimate of the convergence rate $O(1/T)$ in finite dimensions for the complete class of problems.

Second, by fixing $\{\boldsymbol{N}_{(i)}\}_{i=1}^n$, $\{\boldsymbol{R}_{(i)}\}_{i=1}^n$, $\{\boldsymbol{X}_{(i)}\}_{i=1}^n$, the subproblem of $\{\boldsymbol{M}_{(i)}\}_{i=1}^n$, can be written as the following problem,

$$\min_{\{\boldsymbol{M}_{(i)}\}_{i=1}^n} \sum_{i=1}^n \left(\frac{1}{n}\|\boldsymbol{M}_{(i)}\|_{\gamma,r} + \frac{\rho_3}{2}\left\|\boldsymbol{M}_{(i)} - \boldsymbol{X}_{(i)} + \frac{\Lambda_{3(i)}}{\rho_3}\right\|_F^2 \right) \tag{28}$$

which is a non-convex problem [33], let $\phi(\sigma_s(\boldsymbol{M}_{(i)})) = 1 - e^{-\sigma_s(\boldsymbol{M}_{(i)})/\gamma}$, so $\Sigma_{s=r+1}^{min(p,q)}\phi(\sigma_s(\boldsymbol{M}_{(i)}))$ is the nonconvex surrogate of the rank function. $\boldsymbol{M}_{(i)}$ can be represented as $\boldsymbol{M}_{(i)} = \sum_{s=1}^{\min(p,q)}\sigma_s u_s v_s^T$, σ_s is the s-th singular value of matrix $\boldsymbol{M}_{(i)}$, $\nabla\phi(\sigma_s)$ denotes the gradient of ϕ at σ_s. Let $f(\boldsymbol{M}_{(i)}) = \frac{1}{2}\|\boldsymbol{M}_{(i)} - G_{(i)}\|_F^2$ with $G_{(i)} = \boldsymbol{X}_{(i)} - \frac{\Lambda_{3(i)}}{\rho_3}$. It is obvious that the gradient of $f(\boldsymbol{M}_{(i)})$ is Lipschitz continuous by setting the Lipschitz constant being 1. So, the M-subproblem can be written as the following problem,

$$\min_{\{\boldsymbol{M}_{(i)}\}_{i=1}^n} \sum_{i=1}^n \left(\frac{1}{n}\sum_{s=r+1}^{min(p,q)}\phi(\sigma_s(\boldsymbol{M}_{(i)})) + \rho_3 f(\boldsymbol{M}_{(i)}) \right) \tag{29}$$

The penalty function ϕ and loss function f satisfy the following conditions:

A 1: $\phi : \mathbb{R}^+ \to \mathbb{R}^+$ is continuous, concave, monotonically increasing at $[0, \infty)$.

A 2: $f : \mathbb{R}^{p,q} \to \mathbb{R}^+$ is a smooth function and Lipschitz continuous,

$$\|\nabla f(M) - \nabla f(G)\|_F \le L(f)\|M - G\|_F \tag{30}$$

where $L(f)$ is Lipschitz constant of ∇f.

By the supergradient definition of the concave function, we have

$$\phi(\sigma_s(\boldsymbol{M}_{(i)})) \le \phi(\sigma_s) + \nabla\phi(\sigma_s)(\sigma_s(\boldsymbol{M}_{(i)}) - \sigma_s) \tag{31}$$

where

$$0 \le \nabla\phi(\sigma_1) \le \nabla\phi(\sigma_2) \le \ldots \le \nabla\phi(\sigma_s) \tag{32}$$

It is worth noting that the nonnegativeness of $\nabla\phi(\sigma_s)$ is automatically calculated property of ϕ in condition $\boldsymbol{A1}$.

Thus, motivated by (31), we can get the following relaxation problem:

$$\begin{aligned}\boldsymbol{M}_{(i)} &= \frac{1}{\rho_3}\sum_{i=r+1}^{\min(p,q)}\phi(\sigma_s) + \nabla\phi(\sigma_s)(\sigma_s(\boldsymbol{M}_{(i)}) - \sigma_s) + f(\boldsymbol{M}_{(i)}) \\ &= \frac{1}{\rho_3}\sum_{i=r+1}^{\min(p,q)}\nabla\phi(\sigma_s)\sigma_s(\boldsymbol{M}_{(i)}) + f(\boldsymbol{M}_{(i)})\end{aligned} \tag{33}$$

Lemma 1: Given data $G_{(i)} = \boldsymbol{X}^{(i)} - \frac{\Lambda_{3(i)}}{\rho_3}$, $\zeta = min(p, q)$ $0 \le \nabla\phi(\sigma_1) \le \nabla\phi(\sigma_2) \le \ldots \le \nabla\phi(\sigma_\zeta)$, a globally optimal solution $\boldsymbol{M}_{(i)}$ to problem (33) is given by the Weighted Singular Value Thresholding (WSVT) [34]:

$$\boldsymbol{M}_{(i)} = U(\Sigma_{1:r} + S_{\frac{\nabla\phi}{\rho}}(\Sigma_{r+1:\zeta})V^T \tag{34}$$

where $G_{(i)} = U\Sigma V^T$ is SVD of $G_{(i)}$, $\Sigma_{1:r} = diag(\sigma_1, \sigma_2, \ldots, \sigma_r, 0)$, $\Sigma_{r+1:\zeta} = diag(0, \sigma_{r+1}, \ldots, \sigma_\zeta)$ and $S_{\frac{\nabla\phi}{\rho_3}}(\Sigma) = diag\{(\Sigma_{ss} - (\nabla\phi(\sigma_s)/\rho_3))_+\}$.

Third, by fixing $\{\boldsymbol{N}_{(i)}\}_{i=1}^n$, $\{\boldsymbol{M}_{(i)}\}_{i=1}^n$, $\{\boldsymbol{X}_{(i)}\}_{i=1}^n$, the subproblem of $\{\boldsymbol{R}_{(i)}\}_{i=1}^n$, can be written as the following problem,

$$\begin{aligned}\min_{\{\boldsymbol{R}_{(i)}\}_{i=1}^n} &\sum_{i=1}^n \lambda\frac{\rho_1}{2}\left\|\boldsymbol{N}_{(i)} - \boldsymbol{R}_{(i)} + \frac{\Lambda_{1(i)}}{\rho_1}\right\|_F^2 \\ &+ \sum_{i=1}^n \lambda\frac{\rho_2}{2}\left\|\boldsymbol{R}_{(i)} - \boldsymbol{X}_{(i)} + \frac{\Lambda_{2(i)}}{\rho_2}\right\|_F^2\end{aligned} \tag{35}$$

Hence, by solving the minimization problem, the following updated formula can be obtained:

$$\boldsymbol{R}_{(i)} = (\rho_1 I + \rho_2 I)^{-1}(\Lambda_{1(i)} + \rho_1 \boldsymbol{N}_{(i)} + \rho_2 \boldsymbol{X}_{(i)} - \Lambda_{2(i)}) \quad (36)$$

where I stands for the identify matrix.

Finally, the optimization problem w.r.t. $\boldsymbol{\mathcal{X}}$ is:

$$\begin{aligned} &\min_{\boldsymbol{\mathcal{X}}} \sum_{i=1}^{n} \lambda \left(\frac{\rho_2}{2} \left\| \boldsymbol{R}_{(i)} - \boldsymbol{X}_{(i)} + \frac{\Lambda_{2(i)}}{\rho_2} \right\|_F^2 \right) \\ &+ \sum_{i=1}^{n} \left(\frac{\rho_3}{2} \left\| \boldsymbol{M}_{(i)} - \boldsymbol{X}_{(i)} + \frac{\Lambda_{3(i)}}{\rho_3} \right\|_F^2 \right) \\ &s.t. \boldsymbol{\mathcal{X}}_{\Omega} = \boldsymbol{\mathcal{Y}}_{\Omega} \end{aligned} \quad (37)$$

The updated formulae of $\boldsymbol{\mathcal{X}}$ are computed as:

$$\begin{aligned} &\boldsymbol{\mathcal{X}}_{\bar{\Omega}} \\ &= \left[\frac{\sum_{i=1}^{n} (\text{fold}_{(i)}(\Lambda_{3(i)} + \rho_3 \boldsymbol{M}_{(i)})) + \text{fold}_{(i)}(\Lambda_{2(i)} + \rho_3 \boldsymbol{R}_{(i)})}{\left(n\rho_3 + \sum_{i=1}^{n} \lambda_{(i)} \rho_2\right)} \right]_{\bar{\Omega}} \end{aligned}$$

and $\boldsymbol{\mathcal{X}}_{\Omega}$

$$= \boldsymbol{\mathcal{Y}}_{\Omega} \quad (38)$$

Here $\text{fold}_{(i)}(\cdot)$ denotes the opposite operation of mode-n unfolding of a tensor, i.e., $\text{fold}_{(i)}(\boldsymbol{A}_{(i)}) = \boldsymbol{\mathcal{A}}$.

Algorithm 2 The LRRSTV for Tensor Completion

Require: an incomplete tensor $\boldsymbol{\mathcal{Y}}$, iteration number T,λ, ρ_1, ρ_2, ρ_3 and $\mu \in [1, 1.5]$.

Ensure: a recovery tensor $\boldsymbol{\mathcal{X}}$.

1: $[\boldsymbol{\mathcal{X}}]_{\Omega} = [\boldsymbol{\mathcal{Y}}]_{\Omega}$,$[\boldsymbol{\mathcal{X}}]_{\bar{\Omega}} = 0$,randomly initialize $\{\boldsymbol{N}_{(i)}\}_{i=1}^{n}$, $\{\boldsymbol{R}_{(i)}\}_{i=1}^{n}$,$\{\boldsymbol{M}_{(i)}\}_{i=1}^{n}$.
2: **For** $t = 1$ to T **do**
3: Update $\{\boldsymbol{N}_{(i)}\}_{i=1}^{n}$, $\{\boldsymbol{M}_{(i)}\}_{i=1}^{n}$,$\{\boldsymbol{R}_{(i)}\}_{i=1}^{n}$ and $\boldsymbol{\mathcal{X}}$ by equation (24), (34), (36), (38), respectively.
4: $\{\Lambda_{1(i)}\}_{i=1}^{n} = \{\Lambda_{1(i)} + \rho_1(\boldsymbol{N}_{(i)} - \boldsymbol{R}_{(i)})\}_{i=1}^{n}$
5: $\{\Lambda_{2(i)}\}_{i=1}^{n} = \{\Lambda_{2(i)} + \rho_2(\boldsymbol{R}_{(i)} - \boldsymbol{X}_{(i)}\}_{i=1}^{n}$
6: $\{\Lambda_{3(i)}\}_{i=1}^{n} = \{\Lambda_{3(i)} + \rho_3(\boldsymbol{M}_{(i)} - \boldsymbol{X}_{(i)}\}_{i=1}^{n}$
7: $\rho_1 = \mu\rho_1$, $\rho_2 = \mu\rho_2$, $\rho_3 = \mu\rho_3$.
8: $t = t + 1$
9: **Return** $\boldsymbol{\mathcal{X}}$.

Inspired by these update formulae, the whole optimization procedure of our method is given in Algorithm 2. According to the previous derivations, the solving procedure updates the auxiliary matrices $\{\boldsymbol{N}_{(i)}\}_{i=1}^{n}$, $\{\boldsymbol{M}_{(i)}\}_{i=1}^{n}$, $\{\boldsymbol{R}_{(i)}\}_{i=1}^{n}$ and target output variable $\boldsymbol{\mathcal{X}}$ iteratively, which is shown in the third line. In the next 3 lines, the Lagrange multipliers, $\Lambda_{1(i)}$, $\Lambda_{2(i)}$ and $\Lambda_{3(i)}$ are updated following the standard ALADM. In line 7, to accelerate convergence, ρ_1, ρ_2 and ρ_3 are adaptively increased.

IV. PROPOSED MODEL: LRRSTV-T

A. PROBLEM FORMULATION

Tucker decomposition approximates [35] the tensor $\boldsymbol{\mathcal{X}}$ as

$$\boldsymbol{\mathcal{X}} \approx \mathcal{G} \times_1 \boldsymbol{U}^{(1)} \times_2 \boldsymbol{U}^{(2)} \times \ldots_n \boldsymbol{U}^{(n)} \quad (39)$$

where $\boldsymbol{U}^{(n)} \in \mathbb{R}^{I_n \times J_n}$ are matrices of dimensions $I_n \times J_n$ and $\mathcal{G} \in \mathbb{R}^{J_1 \times J_2 \times \ldots \times J_n}$ is N-order tensor. The core tensor $\mathcal{G}$ is solely determined by the factor matrices, with dimensions $J_1 \times J_2 \times \ldots \times J_n$. This process is similar to discovering the low-rank approximation, where $J_1 \times J_2 \times \ldots \times J_n$ are the ranks of the reduced representation.

In our method, to further improves the accuracy, we consider incorporating STV regularization and Schatten-p norm into tensor Tucker decomposition (LRRSTV-T). Specifically, the proposed method is formulated as follow:

$$\begin{aligned} &\min_{\boldsymbol{\mathcal{X}}} \beta_i \sum_{i=1}^{n} \lambda_1 \text{STV}(\boldsymbol{X}_{(i)}) + \frac{1}{n} \sum_{i=1}^{n} \left\| \boldsymbol{U}^{(i)} \right\|_{\gamma,r} + \lambda_2 \|\mathcal{G}\|_F^2 \\ &s.t. \boldsymbol{\mathcal{X}}_{\Omega} = \boldsymbol{\mathcal{Y}}_{\Omega}, \boldsymbol{\mathcal{X}} = \mathcal{G} \times_1 \boldsymbol{U}^{(1)} \times_2 \boldsymbol{U}^{(2)} \times \ldots \times_n \boldsymbol{U}^{(n)} \end{aligned} \quad (40)$$

Similar to LRRSTV, tensor $\boldsymbol{\mathcal{X}}$ represents the recovery result, $\boldsymbol{\mathcal{Y}}$ is an incomplete tensor, $\mathcal{G}$ and $\boldsymbol{U}^{(n)}$ are Tucker decomposition factors. Our cost function in equation (40), comprises of three terms, the first term is STV regularization. The Tucker decomposition factor can be formulated as the second item of this formula because the rank of the factor is sufficiently low. The function of the last term of the formula is to avoid the problem of overfitting in the process of model training.

B. ALGORITHM OPTIMIZATION

In method LRRSTV-T, the three terms are interdependent. To address this problem, we introduce $\{\boldsymbol{N}_{(i)}\}_{i=1}^{n}$, $\{\boldsymbol{R}_{(i)}\}_{i=1}^{n}$ and $\{\boldsymbol{U}^{(i)}\}_{i=1}^{n}$ as auxiliary variables and split the interdependencies and rewrite the optimization problem as

$$\begin{aligned} &\min_{\boldsymbol{\mathcal{X}}, \mathcal{G}, \{\boldsymbol{N}_{(i)}, \boldsymbol{U}^{(i)}\}_{i=1}^{n}} \beta_i \sum_{i=1}^{n} \lambda_1 \text{STV}(\boldsymbol{N}_{(i)}) + \frac{1}{n} \sum_{i=1}^{n} \left\| \boldsymbol{U}^{(i)} \right\|_{\gamma,r} \\ &+ \lambda_2 \|\mathcal{G}\|_F^2 \\ &s.t. \{\boldsymbol{V}^{(i)} = \boldsymbol{U}^{(i)}, \boldsymbol{N}_{(i)} = \boldsymbol{R}_{(i)}, \boldsymbol{R}_{(i)} = \boldsymbol{X}_{(i)}\}_{i=1}^{n} \\ &\boldsymbol{\mathcal{X}}_{\Omega} = \boldsymbol{\mathcal{Y}}_{\Omega}, \boldsymbol{\mathcal{X}} = \mathcal{G} \times_1 \boldsymbol{U}^{(1)} \times_2 \boldsymbol{U}^{(2)} \times \ldots \times_n \boldsymbol{U}^{(n)} \end{aligned} \quad (41)$$

We follow ALADM algorithm to solve the cost function in equation (41). And by using the augmented Lagrange formulation, the optimization problem is transformed into

$$\begin{aligned} \mathcal{L} = &\sum_{i=1}^{n} \lambda_1 \left(\beta_i \text{STV}(\boldsymbol{N}_{(i)}) + \frac{\rho_1}{2} \left\| \boldsymbol{N}_{(i)} - \boldsymbol{R}_{(i)} + \frac{\Lambda_{1(i)}}{\rho_1} \right\|_F^2 \right) \\ &+ \sum_{i=1}^{n} \beta_i \left(\frac{\rho_2}{2} \left\| \boldsymbol{R}_{(i)} - \boldsymbol{X}_{(i)} + \frac{\Lambda_{2(i)}}{\rho_2} \right\|_F^2 \right) + \lambda_2 \|\mathcal{G}\|_F^2 \\ &+ \sum_{i=1}^{n} \left(\frac{1}{n} \|\boldsymbol{U}^{(i)}\|_{\gamma,r} + \frac{\rho_3}{2} \left\| \boldsymbol{V}^{(i)} - \boldsymbol{U}^{(i)} + \frac{\Lambda_{3(i)}}{\rho_3} \right\|_F^2 \right) \end{aligned}$$

$$+\frac{\rho_4}{2}\|\mathcal{X}-\mathcal{G}\times_1 \boldsymbol{V}^{(1)}\times_2 \boldsymbol{V}^{(2)}\times\ldots\times_n \boldsymbol{V}^{(n)}+\frac{\mathcal{Z}}{\rho_4}\|_F^2$$
$$s.t.\mathcal{X}_\Omega=\mathcal{Y}_\Omega \tag{42}$$

where matrices $\{\Lambda_{1(i)}\}_{i=1}^n$, $\{\Lambda_{2(i)}\}_{i=1}^n$, $\{\Lambda_{3(i)}\}_{i=1}^n$ and tensor $\mathcal{Z}$ are Lagrange multipliers. It is easy to check that $\{\boldsymbol{N}_{(i)}\}_{i=1}^n$, $\{\boldsymbol{R}_{(i)}\}_{i=1}^n$, $\{\boldsymbol{U}^{(i)}\}_{i=1}^n$ can be solved as the optimization method LRRSTV.

Fixing $\{\boldsymbol{N}_{(i)}\}_{i=1}^n$, $\{\boldsymbol{R}_{(i)}\}_{i=1}^n$, $\{\boldsymbol{X}_{(i)}\}_{i=1}^n$, $\{\boldsymbol{U}^{(i)}\}_{i=1}^n$ and $\mathcal{G}$, the subproblem of $\{\boldsymbol{V}^{(i)}\}_{i=1}^n$ can be formulated as follows.

$$\min_{\{\boldsymbol{V}^{(i)}\}_{i=1}^n}\sum_{i=1}^n\frac{\rho_3}{2}\left\|\boldsymbol{V}^{(i)}-\boldsymbol{U}^{(i)}+\frac{\Lambda_{3(i)}}{\rho_3}\right\|_F^2$$
$$+\frac{\rho_4}{2}\|\mathcal{X}-\mathcal{G}\times_1 \boldsymbol{V}^{(1)}\times_2 \boldsymbol{V}^{(2)}\times\ldots\times_n \boldsymbol{V}^{(n)}+\frac{\mathcal{Z}}{\rho_4}\|_F^2 \tag{43}$$

Hence, by solving the minimization problem, the following updated formula can be obtained:

$$\boldsymbol{V}^{(i)}=\left(-\Lambda_{3(i)}+\rho_3\boldsymbol{U}^{(i)}+\left(\boldsymbol{Z}_{(i)}+\rho_4\boldsymbol{X}_{(i)}\right)\boldsymbol{V}^{(-i)}\boldsymbol{G}_{(i)}^T\right)$$
$$\times\left(\rho_3 I+\rho_4\boldsymbol{G}_{(i)}\boldsymbol{V}^{(-i)^T}\boldsymbol{V}^{(-i)}\boldsymbol{G}_{(i)}^T\right)^{-1} \tag{44}$$

Similarly, the optimization problem w.r.t. $\mathcal{X}$ is

$$\min_{\mathcal{X}}\sum_{i=1}^n\beta_i\left(\frac{\rho_2}{2}\left\|\boldsymbol{R}_{(i)}-\boldsymbol{X}_{(i)}+\frac{\Lambda_{2(i)}}{\rho_2}\right\|_F^2\right)$$
$$+\frac{\rho_4}{2}\|\mathcal{X}-\mathcal{G}\times_1 \boldsymbol{V}^{(1)}\times_2 \boldsymbol{V}^{(2)}\times\ldots\times_n \boldsymbol{V}^{(n)}+\frac{\mathcal{Z}}{\rho_4}\|_F^2$$
$$s.t.\mathcal{X}_\Omega=\mathcal{Y}_\Omega \tag{45}$$

Then $\mathcal{X}$ can be computed as

$$\boldsymbol{X}_{\bar{\Omega}}=\left[\frac{\sum_{i=1}^n\beta_i\left(-\text{fold}_{(i)}(\Lambda_{2(i)}+\rho_2\boldsymbol{R}_{(i)})\right)-\boldsymbol{Z}+\rho_4\hat{\mathcal{X}}}{\sum_{i=1}^n\beta_i\rho_2+\rho_4}\right]$$
$$\text{and } \mathcal{X}_\Omega=\boldsymbol{Y}_\Omega \tag{46}$$

Finally, we can compute $\mathcal{G}$ as

$$\text{vec}(\mathcal{G})=\left(\boldsymbol{V}^{(-i)^T}\boldsymbol{V}^{(-i)}\otimes\rho_4\boldsymbol{V}^{(i)^T}\boldsymbol{V}^{(-i)^T}+\lambda_2 I\right)^{-1}$$
$$\left(\text{vec}\boldsymbol{V}^{(-i)^T}(\boldsymbol{Z}_{(i)}+\rho_4\boldsymbol{X}_{(i)})\boldsymbol{V}^{(-i)}\right) \tag{47}$$

where $\otimes$ is the Kronecker product, $\boldsymbol{V}^{(-i)}=\boldsymbol{V}^{(1)}\otimes\boldsymbol{V}^{(2)}\otimes\ldots\otimes\boldsymbol{V}^{(i-1)}\otimes\boldsymbol{V}^{(i+1)}\otimes\ldots\boldsymbol{V}^{(i)}$, and in equation (46), $\hat{\mathcal{X}}=\mathcal{G}\times_1\boldsymbol{V}^{(1)}\times_2\boldsymbol{V}^{(2)}\times\ldots\times_n\boldsymbol{V}^{(n)}$. With the above update formulae, we summarize the solver of our method in Algorithm 3.

Algorithm 3 The LRRSTV-T for Tensor Completion

Require: an incomplete tensor $\mathcal{Y}$, iteration number T,λ_1, λ_2, ρ_1, ρ_2, ρ_3, ρ_4 and $\mu\in[1, 1.5]$.
Ensure: a recovery tensor $\mathcal{X}$.
1: $[\mathcal{X}]_\Omega=[\mathcal{Y}]_\Omega$,$[\mathcal{X}]_{\bar{\Omega}}=0$,randomly initialize $\{\boldsymbol{N}_{(i)}\}_{i=1}^n$, $\{\boldsymbol{R}_{(i)}\}_{i=1}^n$,$\{\boldsymbol{M}_{(i)}\}_{i=1}^n$.
2: **For** $t=1$ to T **do**
3: Update $\{\boldsymbol{N}_{(i)}\}_{i=1}^n$, $\{\boldsymbol{U}^{(i)}\}_{i=1}^n$, $\{\boldsymbol{R}_{(i)}\}_{i=1}^n$,$\{\boldsymbol{V}^{(i)}\}_{i=1}^n$,$\mathcal{X}$ and $\mathcal{G}$ by equation (24), (34), (36), (44), (46),(47) respectively.
4: $\{\Lambda_{1(i)}\}_{i=1}^n=\{\Lambda_{1(i)}+\rho_1(\boldsymbol{N}_{(i)}-\boldsymbol{R}_{(i)})\}_{i=1}^n$
5: $\{\Lambda_{2(i)}\}_{i=1}^n=\{\Lambda_{2(i)}+\rho_2(\boldsymbol{R}_{(i)}-\boldsymbol{X}_{(i)}\}_{i=1}^n$
6: $\{\Lambda_{3(i)}\}_{i=1}^n=\{\Lambda_{3(i)}+\rho_3(\boldsymbol{V}^{(i)}-\boldsymbol{U}^{(i)}\}_{i=1}^n$
7: $\mathcal{Z}=\mathcal{Z}+\mathcal{G}\times_1\boldsymbol{V}^{(1)}\times_2\boldsymbol{V}^{(2)}\times\ldots\times_n\boldsymbol{V}^{(n)}$
8: $\rho_1=\mu\rho_1$, $\rho_2=\mu\rho_2$, $\rho_3=\mu\rho_3$, $\rho_4=\mu\rho_4$.
9: $t=t+1$
10: **Return** $\mathcal{X}$.

V. EXPERIMENTAL RESULTS

We apply our methods to a variety of natural images with different inpainting tasks, i.e. text removal, and randomly missing pixels filling. Specifically, we compare our approaches, i.e., LRRSTV and LRRSTV-T, with some recently presented algorithms, including HaLRTC [18], FBCP [22], FBCP-MF, LRTC-TV-II [20]. The first eight benchmark color images for the experiment are shown in Fig. 4. Each of them has three color channels and the resolution of each one is 256-by-256. In a word, they can be represented as 256-by-256-by-3 tensors. In order to better compare the effects from different algorithm in different dataset, we add two more Paris Streetview color images whose resolution both are 227-by-227. The well-known evaluation metrics, Peak Signal to Noise Ratio (PSNR) and Structural Similarity (SSIM) indices are adopted to demonstrate the performance of all the competing methods. The computation formulations of PSNR and SSIM are as follows

$$\text{PSNR}=10\times\lg\frac{mn}{\sum_{x=1}^m\sum_{y=1}^n[B(x,y)-A(x,y)]^2} \tag{48}$$

$$\text{SSIM}=\frac{(2\mu_A\mu_B+C_1)(2\sigma_{AB}+C_2)}{(\mu_A^2+\mu_B^2+C_1)(\sigma_A^2+\sigma_B^2+C_2)} \tag{49}$$

where B indicates the recovered image and A indicates the ground truth. The larger values of PSNR and SSIM indicate better recovery performance. For fairness, the tunable parameters of each algorithm are finely set such that the results of quantitative criteria, visual assessment, and computational cost of each algorithm are optimal. For fairness, the tunable parameters of each algorithm are finely set such that the results of quantitative criteria, visual assessment, and computational cost of each algorithm are optimal. Furthermore, the maximum iteration number and the stop tolerance are set as 200 and 1e-5, respectively. For our method, we set

FIGURE 4. Ground truth of color images.

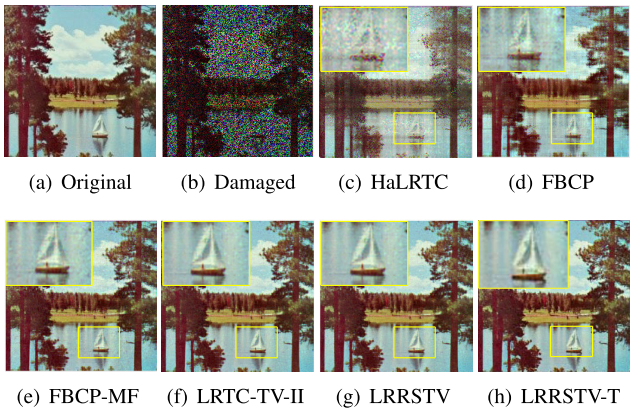

(a) Original (b) Damaged (c) HaLRTC (d) FBCP

(e) FBCP-MF (f) LRTC-TV-II (g) LRRSTV (h) LRRSTV-T

FIGURE 5. Recovery results of (c) HaLRTC, (d) FBCP, (e) FBCP-MF, (f) LRTC-TV-II, (g) LRRSTV and (h)LRRSTV-T methods on the 60% random missing image "sailboat".

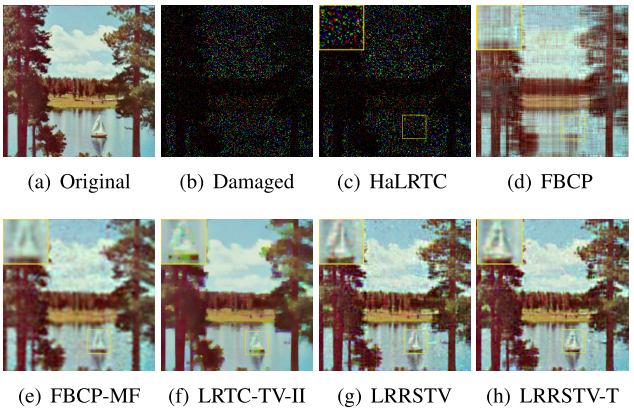

(a) Original (b) Damaged (c) HaLRTC (d) FBCP

(e) FBCP-MF (f) LRTC-TV-II (g) LRRSTV (h) LRRSTV-T

FIGURE 6. Recovery results of (c) HaLRTC, (d)FBCP, (e) FBCP-MF, (f) LRTC-TV-II, (g) LRRSTV and (h)LRRSTV-T methods on the 90% random missing image "sailboat".

$\lambda = \lambda_1 = 1, \lambda_2 = 0$ and $\beta = 2.0 \times 10^{-2}$ in all the experiments.

Experimental environment: CPU for Intel (R) Core i7-7500U 2.70GHz, 8GB of memory capacity, the system is 64-bit Microsoft Windows 10, the software version is Matlab R2016a.

A. EXPERIMENTS ON RANDOM PIXELS MISSING

In this subsection, to test the inpainting performance, a benchmark color image "sailboat" with 60% and 90% missing pixels and a Paris StreetView color image with 90% missing pixels are considered as observed samples. Fig.5 presents the recovery results on image "sailboat" with 60% random missing pixels. The performances on image "sailboat" and the Paris StreetView color image with 90% random missing pixels are shown in Fig.6 and Fig.7, respectively. Obviously, the worst perceptual results are the ones from HaLRTC, whose recovered images contain several vertical or horizontal noisy lines and also many other artifacts. The reason for the worst performance is that the local smooth and piecewise property of visual data is neglected in HaLRTC. LRTC-TV-II, a model based on Tucker decomposition and total variation, outperforms most other competitors benefiting from its additionally introduced variables for achieving better recovery results. However, it still lacks behind LRRSTV-T due to our deeper consideration of the low-rank and smooth properties.

To measure experimental results from an objective perspective, Table 1 and Table 2 list the numerical results on image "sailboat" under random missing ratios of 60%, and 90%, respectively. Table 3 lists the quantitative metrics on the Paris StreetView color image with 90% random missing pixels. We can get similar results from these tables, HaLRTC again performs the worst and our method LRRSTV-T performs the best among all the approaches. Although the performance gap under random missing ratio 60% is marginal, it can be clearly observed that when the random missing ratio is 90%, our advantage is quite encouraging. In the

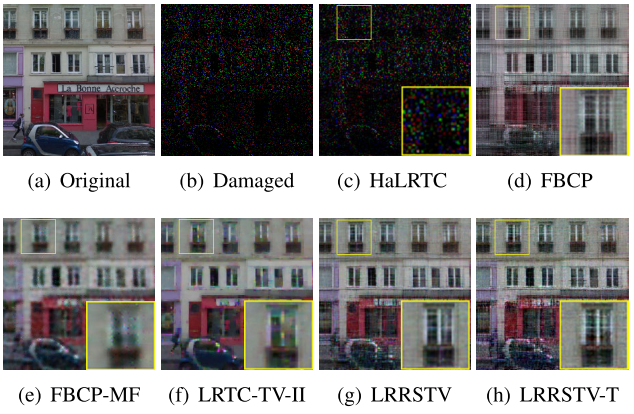

(a) Original (b) Damaged (c) HaLRTC (d) FBCP

(e) FBCP-MF (f) LRTC-TV-II (g) LRRSTV (h) LRRSTV-T

FIGURE 7. Example results on the 90% random missing, compared to c) HaLRTC, (d)FBCP, (e) FBCP-MF, (f) LRTC-TV-II, on the Paris StreetView dataset.

magnified views of the yellow box in Fig. 5, we can observe that compared with LRRSTV and LRTC-TV-II, LRRSTV can better describe the edge of the boat mast. Even, on the whole, the results recovered by algorithm LRRSTV are a little more ambiguous compared with algorithm LRTC-TV-II.

To comprehensively investigate the performance of different competing methods, we further randomly remove 55%, 60%, 65%,70%, 75%, 80%, 85%, and 90% points in first eight benchmark color images as missing values, then compute the average recovery results. Fig.8 illustrates the PSNR value versus increasing mask ratios of different approaches. We can see that our method LRRSTV-T performs the best, other algorithms' performances become much worse when the missing rate is dropping from 55% to 90%. It can be seen that the LRRSTV-T method prevailed over other algorithms in performance.

B. EXPERIMENTS ON TEXT REMOVAL

Text removal is another important problem in image processing. The comparisons of different algorithms on text removal task applied to image "peppers",image "baboon" and the

TABLE 1. Recovery results by Various Completion Methods on the 60% random missing image "sailboat".

Methods	HaLRTC	FBCP	FBCP-MF	LRTC-TV-II	LRRSTV	LRRSTV-T
PSNR	23.02	24.93	26.09	27.65	27.24	28.39
SSIM	0.684	0.790	0.883	0.916	0.902	0.943

TABLE 2. Recovery results by Various Completion Methods on the 90% random missing image "sailboat".

Methods	HaLRTC	FBCP	FBCP-MF	LRTC-TV-II	LRRSTV	LRRSTV-T
PSNR	16.02	18.65	21.45	21.07	20.65	21.81
SSIM	0.156	0.433	0.667	0.706	0.694	0.719

TABLE 3. Recovery results on the 90% random missing, compared to Various Completion Methods, on the Paris StreetView dataset.

Methods	HaLRTC	FBCP	FBCP-MF	LRTC-TV-II	LRRSTV	LRRSTV-T
PSNR	7.10	21.34	21.88	23.27	23.32	23.61
SSIM	0.122	0.617	0.621	0.746	0.733	0.767

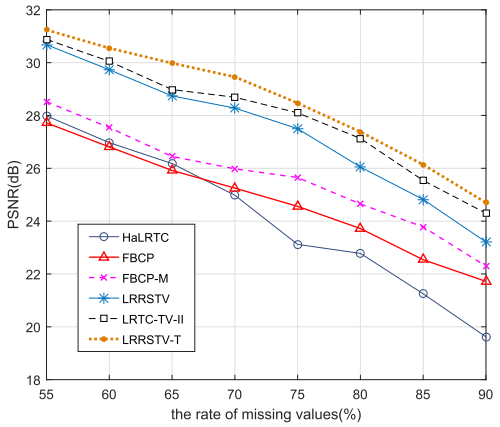

FIGURE 8. Average recovery results of methods on the 55%-90% random missing image.

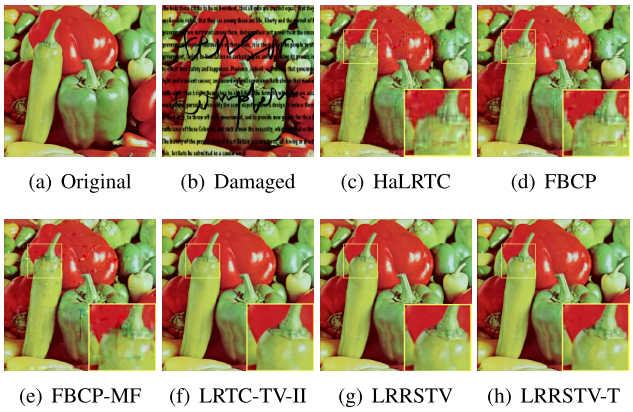

(a) Original (b) Damaged (c) HaLRTC (d) FBCP

(e) FBCP-MF (f) LRTC-TV-II (g) LRRSTV (h) LRRSTV-T

FIGURE 9. Recovery results of (c) HaLRTC, (d) FBCP, (e) FBCP-MF, (f) LRTC-TV-II,(g) LRRSTV and (h)LRRSTV-T methods on text removal image "peppers".

TABLE 4. Recovery results by Various Completion Methods on text removal image "peppers".

Methods	HaLRTC	FBCP	FBCP-MF	LRTC-TV-II	LRRSTV	LRRSTV-T
PSNR	24.34	27.81	28.73	32.64	31.39	33.42
SSIM	0.743	0.875	0.903	0.966	0.958	0.971

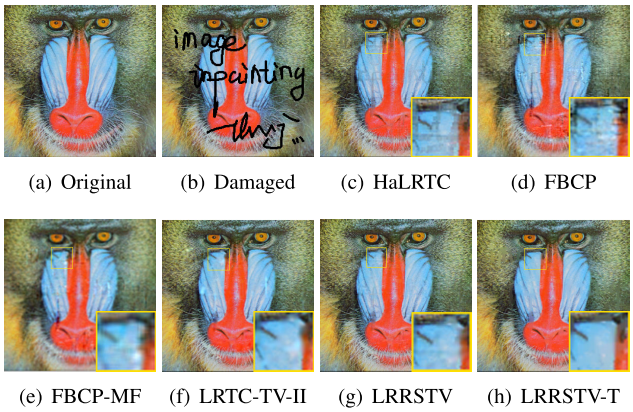

(a) Original (b) Damaged (c) HaLRTC (d) FBCP

(e) FBCP-MF (f) LRTC-TV-II (g) LRRSTV (h) LRRSTV-T

FIGURE 10. Recovery results of (c) HaLRTC, (d) FBCP, (e) FBCP-MF, (f) LRTC-TV-II,(g) LRRSTV and (h)LRRSTV-T methods on text removal image "baboon".

Paris StreetView image are respectively shown in Fig.9, Fig.10 and Fig.11, respectively. The corresponding numerical results, namely PSNR and SSIM, are shown in Table 4, Table 5 and Table 6, respectively. From these results, roughly speaking, the image with damaged structure and texture information can be recovered by all the selected algorithms both visually and quantitatively.

From a deeper insigh, it can be observed in Fig.9 that although the damaged image can be repaired by HaLRTC in general, there are still some serious error or ambiguities in the restoration of the texture information, especially around the damaged region. From a subjective visual perspective, the text region removed through our method is much closer to the original image. In addition, according to the evaluation indexes, the performance of our method is also better than others on these text corrupted color images.

The results of Fig. 10 also show the improvement of our method LRRSTV-T over the others. In the magnified views of the yellow box, we can observe that HaLRTC, FBCP and FBCP-MF still have much residual shadow of the scratches. We attribute it to the fact that these algorithms ignore local smoothness and segmentation of natural images. Algorithm LRTC-TV-II achieve similar results to our algorithm, but it produces many undesirable artifacts. The performances on the text corrupted Paris StreetView color image are shown in Fig.11. This experiment demonstrates that our algorithms can effectively fill the missing information. Overall, our method not only fills the desirable pixels but also preserves sharper edges and finer details, showing better visual quality than the other competing methods.

C. COMPONENT ANALYSIS

Besides the introduced jointly optimization scheme, which results in better PSNR results and appealing efficiency for our proposed method, the performance of LRRSTV and

TABLE 5. Recovery results by Various Completion Methods on text removal image "baboon".

Methods	HaLRTC	FBCP	FBCP-MF	LRTC-TV-II	LRRSTV	LRRSTV-T
PSNR	29.48	30.68	30.42	30.83	30.26	31.14
SSIM	0.933	0.947	0.941	0.948	0.942	0.950

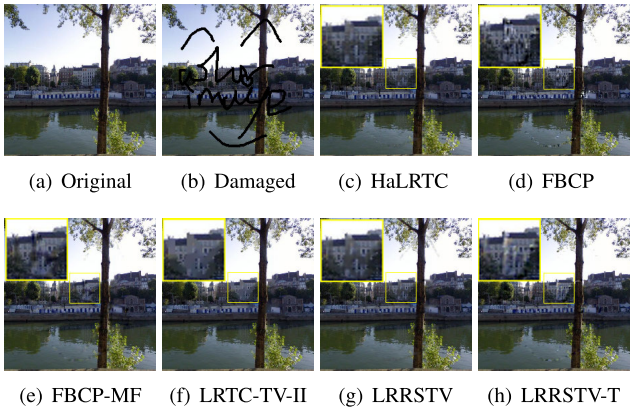

(a) Original (b) Damaged (c) HaLRTC (d) FBCP

(e) FBCP-MF (f) LRTC-TV-II (g) LRRSTV (h) LRRSTV-T

FIGURE 11. Example results on text removal, compared to c) HaLRTC, (d)FBCP, (e) FBCP-MF, (f) LRTC-TV-II, on the Paris StreetView dataset.

TABLE 6. Recovery results on text removal, compared to Various Completion Methods, on the Paris StreetView dataset.

Methods	HaLRTC	FBCP	FBCP-MF	LRTC-TV-II	LRRSTV	LRRSTV-T
PSNR	22.47	27.38	29.76	30.32	30.34	31.52
SSIM	0.840	0.901	0.913	0.946	0.933	0.964

LRRSTV-T also depend on two other components. That is (i) the STV relying on oversampling factor a, and (ii) the truncated γ-norm relying on parameter r. In the previous experiments, we simply fix their values for a fair comparison. Next, we evaluate our algorithm using varing a and r.

Fig. 12 plots the PSNR and runtime curves on images "barbara", "sailboat", "facade" and "airplane" with a traversed in $\{1, 2, \ldots, 5\}$. Note that in Fig.12 (a), our method performs relatively better when a becomes lager. We also observe that the larger the a value, the more runtime required for model convergence. In real-world applications, $a = 3$ is a desirable value for a well balance of effectiveness and efficiency.

Fig. 13 further plots the PSNR and runtime curves on the remaining images with r traversed in $\{0, 1, \ldots, 8\}$. In Fig.13(a), the curves on different images are relatively stable along with the variations of r. In Fig.13(b), though the lines on different images fluctuates with the variation of r, the runtime of our algorithm with $r > 0$ is always less than that when $r = 0$. In practice, we suggest $r = 5$ due to its appealing results on both of effectiveness and efficiency.

Recall that in our proposed model, the low-rank hypothesis and smooth priori are introduced for the purpose of recovering or retaining the intrinsic properties in natural images. In order to analyze which one of the two regularizations plays a more important role in enhancing image quality, we test five images, including "airplane","barbara", "lena", "baboon", "peppers", using "only low-rank regularization

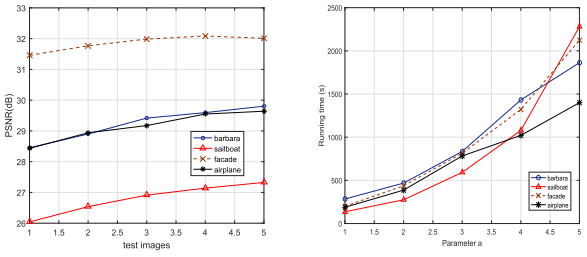

(a) (b)

FIGURE 12. Comparisons on (a) PSNR and (b) running time under different settings of parameter a.

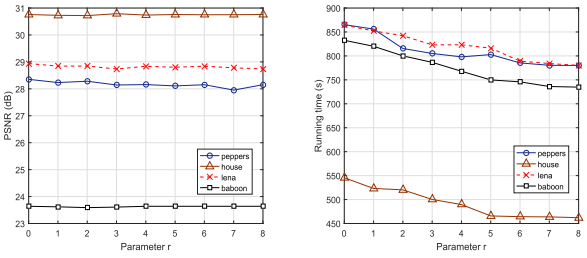

(a) (b)

FIGURE 13. Comparisons on (a) PSNR and (b) running time under different settings of parameter r.

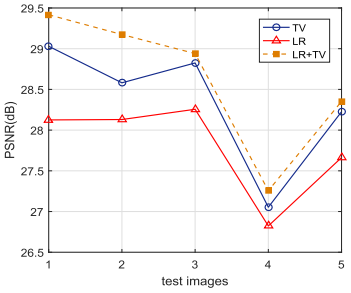

FIGURE 14. Image inpainting performance on five images form the 60% random missing with different regularization.

(LR)", "only smooth regularization (TV)", and "smooth regularization with low-rank prior (LR+TV)", respectively. Fig. 14 shows the experimental results on five images under 60% randomly pixels missing. From this figure, we can observe that LR+TV achieves the highest numerical values in all the images, which demonstrates the advancement of integrating multiple properties into consideration. In addition, the performance of LR is consistently poorer than the one from TV, which verifies the superiority of Shannon interpolation operation.

VI. CONCLUSION

In this study, by integrating Shannon total variation and truncated γ-norm into Tucker-based low-rank tensor completion framework, we propose to model together the local smoothness and low rank prior of visual data. Moreover, since that LRTC can be represented by tensor unfolding and tensor decomposition, we Correspondingly develop two

methods, namely LRRSTV and LRRSTV-T, for the image inpainting problem. By considering the color image as a 3-order tensor, our proposed methods can be directly used in this multi-channel completion application. Experiments under three different cases with 10 natural images demonstrate that our proposal in this paper have both subjective and objective advantages respectively in visual effect and numerical metrics. In practice, our approach can achieve high-fidelity recovery from the corrupted images in the edge and texture regions.

The proposed methods are conceptually basic and have great potential for further improvement. One current disadvantage of our algorithms is that they run slowly in images with relatively larger size, e.g., 1024×1024. This is attributed to the huge computational cost of the STV operation. We will focus on solving this issue in the near future by investigating some closed form operator, making our algorithm more efficient.

REFERENCES

[1] C. Guillemot and O. Le Meur, "Image inpainting : Overview and recent advances," *IEEE Signal Process. Mag.*, vol. 31, no. 1, pp. 127–144, Jan. 2014.

[2] J. Yu, Z. Lin, J. Yang, X. Shen, X. Lu, and T. Huang, "Free-form image inpainting with gated convolution," in *Proc. IEEE/CVF Int. Conf. Comput. Vis. (ICCV)*, Oct. 2019, pp. 4471–4480.

[3] M. Bertalmio, G. Sapiro, V. Caselles, and C. Ballester, "Image inpainting," in *Proc. 27th Annu. Conf. Comput. Graph. Interact. Techn.*, 2000, pp. 417–424.

[4] N. Komodakis, "Image completion using global optimization," in *Proc. IEEE Comput. Soc. Conf. Comput. Vis. Pattern Recognit. (CVPR)*, vol. 1, Jun. 2006, pp. 442–452.

[5] M. Oquab, L. Bottou, I. Laptev, and J. Sivic, "Learning and transferring mid-level image representations using convolutional neural networks," in *Proc. IEEE Conf. Comput. Vis. Pattern Recognit.*, Jun. 2014, pp. 1717–1724.

[6] C. Wang, H. Huang, X. Han, and J. Wang, "Video inpainting by jointly learning temporal structure and spatial details," in *Proc. AAAI Conf. Artif. Intell.*, vol. 33, Jul. 2019, pp. 5232–5239.

[7] R. A. Yeh, C. Chen, T. Y. Lim, A. G. Schwing, M. Hasegawa-Johnson, and M. N. Do, "Semantic image inpainting with deep generative models," in *Proc. IEEE Conf. Comput. Vis. Pattern Recognit. (CVPR)*, Jul. 2017, pp. 5485–5493.

[8] Z. Yan, X. Li, M. Li, W. Zuo, and S. Shan, "Shift-net: Image inpainting via deep feature rearrangement," in *Proc. Eur. Conf. Comput. Vis. (ECCV)*, 2018, pp. 1–17.

[9] E. J. Candès and B. Recht, "Exact matrix completion via convex optimization," *Found. Comput. Math.*, vol. 9, no. 6, pp. 717–772, Dec. 2009.

[10] C. Lu, X. Peng, and Y. Wei, "Low-rank tensor completion with a new tensor nuclear norm induced by invertible linear transforms," in *Proc. IEEE/CVF Conf. Comput. Vis. Pattern Recognit. (CVPR)*, Jun. 2019, pp. 5996–6004.

[11] P. Jidesh and I. P. Febin, "Estimation of noise using non-local regularization frameworks for image denoising and analysis," *Arabian J. Sci. Eng.*, vol. 44, no. 4, pp. 3425–3437, Apr. 2019.

[12] A. A. Bini, "Image restoration via DOST and total variation regularisation," *IET Image Process.*, vol. 13, no. 3, pp. 458–468, Feb. 2019.

[13] J. Fan and R. Li, "Variable selection via nonconcave penalized likelihood and its oracle properties," *J. Amer. Stat. Assoc.*, vol. 96, no. 456, pp. 1348–1360, Dec. 2001.

[14] I. Markovsky, "Applications of structured low-rank approximation," *IFAC Proc. Volumes*, vol. 42, no. 10, pp. 1121–1126, 2009.

[15] F. Shang, Y. Liu, and J. Cheng, "Scalable algorithms for tractable schatten quasi-norm minimization," in *Proc. 13th AAAI Conf. Artif. Intell.*, Mar. 2016, pp. 2016–2022.

[16] H. Zhang, J. Yang, F. Shang, C. Gong, and Z. Zhang, "LRR for subspace segmentation via tractable schatten-p norm minimization and factorization," *IEEE Trans. Cybern.*, vol. 49, no. 5, pp. 1722–1734, May 2019.

[17] Y. Chen, Y. Guo, Y. Wang, D. Wang, C. Peng, and G. He, "Denoising of hyperspectral images using nonconvex low rank matrix approximation," *IEEE Trans. Geosci. Remote Sens.*, vol. 55, no. 9, pp. 5366–5380, Sep. 2017.

[18] J. Liu, P. Musialski, P. Wonka, and J. Ye, "Tensor completion for estimating missing values in visual data," *IEEE Trans. Pattern Anal. Mach. Intell.*, vol. 35, no. 1, pp. 208–220, Jan. 2013.

[19] J. D. Hauenstein, L. Oeding, G. Ottaviani, and A. J. Sommese, "Homotopy techniques for tensor decomposition and perfect identifiability," *J. Reine Angew. Math.*, vol. 2019, no. 753, pp. 1–22, Aug. 2019.

[20] X. Li, Y. Ye, and X. Xu, "Low-rank tensor completion with total variation for visual data inpainting," in *Proc. 31st AAAI Conf. Artif. Intell.*, 2017, pp. 2210–2216.

[21] T. Yokota and H. Hontani, "Simultaneous visual data completion and denoising based on tensor rank and total variation minimization and its primal-dual splitting algorithm," in *Proc. IEEE Conf. Comput. Vis. Pattern Recognit. (CVPR)*, Jul. 2017, pp. 3732–3740.

[22] Q. Zhao, L. Zhang, and A. Cichocki, "Bayesian CP factorization of incomplete tensors with automatic rank determination," *IEEE Trans. Pattern Anal. Mach. Intell.*, vol. 37, no. 9, pp. 1751–1763, Sep. 2015.

[23] T. Yokota, Q. Zhao, and A. Cichocki, "Smooth PARAFAC decomposition for tensor completion," *IEEE Trans. Signal Process.*, vol. 64, no. 20, pp. 5423–5436, Oct. 2016.

[24] B. Recht, M. Fazel, and P. A. Parrilo, "Guaranteed minimum-rank solutions of linear matrix equations via nuclear norm minimization," *SIAM Rev.*, vol. 52, no. 3, pp. 471–501, Jan. 2010.

[25] W. Wu, P. Chen, V. V. Vardhanabhuti, W. Wu, and H. Yu, "Improved material decomposition with a two-step regularization for spectral CT," *IEEE Access*, vol. 7, pp. 158770–158781, 2019.

[26] W. Wu, Y. Zhang, Q. Wang, F. Liu, P. Chen, and H. Yu, "Low-dose spectral CT reconstruction using image gradient ℓ_0–norm and tensor dictionary," *Appl. Math. Model.*, vol. 63, pp. 538–557, Nov. 2018.

[27] R. Abergel and L. Moisan, "The Shannon total variation," *J. Math. Imag. Vis.*, vol. 59, no. 2, pp. 341–370, Oct. 2017.

[28] Y. Shen, Z. Wen, and Y. Zhang, "Augmented lagrangian alternating direction method for matrix separation based on low-rank factorization," *Optim. Methods Softw.*, vol. 29, no. 2, pp. 239–263, Mar. 2014.

[29] J. Xu, L. Zhang, D. Zhang, and X. Feng, "Multi-channel weighted nuclear norm minimization for real color image denoising," in *Proc. IEEE Int. Conf. Comput. Vis. (ICCV)*, Oct. 2017, pp. 1096–1104.

[30] T.-Y. Ji, T.-Z. Huang, X.-L. Zhao, T.-H. Ma, and G. Liu, "Tensor completion using total variation and low-rank matrix factorization," *Inf. Sci.*, vol. 326, pp. 243–257, Jan. 2016.

[31] L. Zhou and J. Tang, "Fraction-order total variation blind image restoration based on L1-norm," *Appl. Math. Model.*, vol. 51, pp. 469–476, Nov. 2017.

[32] A. Chambolle and T. Pock, "A first-order primal-dual algorithm for convex problems with applications to imaging," *J. Math. Imag. Vis.*, vol. 40, no. 1, pp. 120–145, May 2011.

[33] B. Wen, X. Chen, and T. K. Pong, "A proximal difference-of-convex algorithm with extrapolation," *Comput. Optim. Appl.*, vol. 69, no. 2, pp. 297–324, Mar. 2018.

[34] S. Gaïffas and G. Lecué, "Weighted algorithms for compressed sensing and matrix completion," 2011, *arXiv:1107.1638*. [Online]. Available: http://arxiv.org/abs/1107.1638

[35] D. Kressner, M. Steinlechner, and B. Vandereycken, "Low-rank tensor completion by Riemannian optimization," *BIT Numer. Math.*, vol. 54, no. 2, pp. 447–468, Jun. 2014.

MENGJIE QIN received the M.S. degree from the School of Computer Science and Engineering, Zhejiang University of Technology, China, in 2018. She is currently pursuing the Ph.D. degree with the Zhejiang University of Technology. Her research interests include image and video enhancement, pattern recognition, and machine learning.

ZHUORONG LI received the Ph.D. degree in control science and engineering from the Zhejiang University of Technology. She is currently a Lecturer with the Zhejiang University City College. Her research interests include computational vision, deep learning and corresponding applications, and machine learning.

SHENGYONG CHEN (Senior Member, IEEE) received the Ph.D. degree in computer vision from the City University of Hong Kong, Hong Kong, in 2003. He worked with the University of Hamburg, from 2006 to 2007. He is currently a Professor with the Tianjin University of Technology and the Zhejiang University of Technology, China. He has published over 100 scientific articles in international journals. His research interests include computer vision, robotics, and image analysis. He is also a Senior Member of CCF and a Fellow of IET. He has received the fellowship from the Alexander von Humboldt Foundation of Germany. He has also received the National Outstanding Youth Foundation Award of China, in 2013.

QIU GUAN received the Ph.D. degree in control theory and control engineering from the College of Computer Science and Technology, Zhejiang University of Technology, in 2012. She is currently a Professor and a Ph.D. Supervisor with the College of Computer Science and Technology, Zhejiang University of Technology. Her research interests include computer vision and medical image processing. In 2007, she was a Visiting Scholar with University College London, U.K., for one year, where she focused her study on medical image processing under the sponsorship of the Chinese Scholarship Council. She has carried out a number of China's state and province funded research projects as a PI or a Co-PI in the area related to these fields, which resulted in a number of papers published in international conference proceedings and journals.

JIANWEI ZHENG received the B.Sc. degree, in 2005, and the Ph.D. degree in control theory and control engineering from the Zhejiang University of Technology, China, in 2010. He is currently an Associate Professor with the School of Computer Science and Engineering, Zhejiang University of Technology. He has published more than 60 academic papers in reputable journals and conferences, including the IEEE TIP, the IEEE TNNLS, the IEEE TII, *Neurocomputing*, *Visual Computer*, *Applied Intelligence*, PCM, and CGI.